Magneto-optical Kerr effect in pump-probe setups

Amir Eskandari-asl [1] and Adolfo Avella [1,2,3]
[1]*Dipartimento di Fisica "E.R. Caianiello," Università degli Studi di Salerno, I-84084 Fisciano (SA), Italy*
[2]*CNR-SPIN, Unità di Salerno, I-84084 Fisciano (SA), Italy*
[3]*CNISM, Unità di Salerno, Università degli Studi di Salerno, I-84084 Fisciano (SA), Italy*

(Received 1 November 2025; accepted 12 January 2026; published 29 January 2026)

We develop a general theoretical framework for computing the time-resolved magneto-optical Kerr effect in ultrafast pump-probe setups, formulated within the dynamical projective operatorial approach (DPOA) and its application to the generalized linear-response theory for pumped systems. Furthermore, we exploit this formalism to express the postpump optical conductivity—and consequently the Kerr rotation—in terms of the time-evolved single-particle density matrix (SPDM), providing a transparent and computationally efficient description of photoexcited multiband systems. This extension, in addition to its lower computational cost, has the advantage of allowing the inclusion of phenomenological damping. We illustrate the formalism using both (1) a two-band tight-binding model, which captures the essential physics of ultrafast spin-charge dynamics and the Kerr rotation and (2) weakly spin-polarized germanium, as a realistic playground with a complex band structure. The results demonstrate that, by exploiting DPOA and/or its SPDM extension, one can reliably reproduce both the short-time features under the pump-pulse envelope and the long-time dynamics after excitation, offering a versatile framework for analyzing time-resolved magneto-optical Kerr effect experiments in complex materials. Moreover, this analysis clearly shows that the Kerr rotation can be used to deduce experimentally the relevant n-photon resonances for a given specific material.

DOI: 10.1103/wfcr-75gl

I. INTRODUCTION

In recent years, the development of ultrafast pump-probe spectroscopy has opened a new frontier in exploring the dynamics of condensed matter systems on femtosecond and even subfemtosecond timescales [1–8]. By monitoring the temporal evolution of photoexcited carriers, these techniques provide direct access to the microscopic mechanisms governing electronic, spin, and lattice degrees of freedom out of equilibrium. From a technological standpoint, such insight is essential for advancing next-generation ultrafast optoelectronic and spintronic devices. From a fundamental perspective, it enables one to probe pulse symmetry breaking, coherence, and relaxation processes in real time [9–11].

Among various ultrafast observables, the time-resolved magneto-optical Kerr effect has emerged as a powerful probe for detecting transient magnetization dynamics and nonequilibrium spin polarization [12]. The Kerr and also Faraday rotations—arising from the off-diagonal components of the optical conductivity tensor—encode information about spin-orbit coupling (SOC) and the instantaneous breaking of time-reversal symmetry (TRS) [13]. They thus provide a direct experimental window into ultrafast processes such as light-induced magnetization, coherent spin precession, and photoinduced topological transitions [14–19]. In systems such as pumped altermagnets or magnetic semiconductors, Kerr rotation measurements serve as a sensitive fingerprint of the evolving symmetry and band topology on ultrafast timescales [20–22].

Despite its experimental relevance, a comprehensive and computationally affordable theoretical framework for evaluating the transient Kerr response has remained elusive [23,24]. *Ab initio* methods based on time-dependent density functional theory are, in principle, capable of describing the pump-probe dynamics [25–27], but their extremely high computational cost and limited interpretability make them unsuitable for exploring a broad parameter space or for isolating the microscopic origin of specific phenomena. Model-Hamiltonian approaches [28–30] can address these issues by allowing controlled manipulation of individual Hamiltonian terms, but they often lack the generality and the complexity required for realistic simulations.

To bridge this gap, we recently developed the dynamical projective operatorial approach (DPOA) [7,31–34], an efficient operator-based formalism for studying ultrafast phenomena in realistic multiband systems. DPOA enables the real-time evolution of composite operators under the action of intense pump fields, while maintaining full access to microscopic observables such as the single-particle density matrix (SPDM), band populations, interband coherences, and in principle, every multitime multiparticle response function, including time-resolved angle-resolved photoemission spectroscopy [31] and transient optical properties, through the generalized linear response theory for pumped systems [32].

Published by the American Physical Society under the terms of the Creative Commons Attribution 4.0 International license. Further distribution of this work must maintain attribution to the author(s) and the published article's title, journal citation, and DOI.

DPOA formulation is, in principle, fully general—applicable to systems with arbitrary lattice structures, numbers of bands, or other complexities.

In the present work, we build upon DPOA to formulate a general theory for computing the transient Kerr rotation in pump-probe setups. Furthermore, we extend the framework to include phenomenological damping within the SPDM dynamics, allowing us to capture relaxation effects that are essential in realistic experimental conditions.

The paper is organized as follows. In Sec. II, we outline the theoretical formulation of the two-time optical conductivity and its reduction in terms of the SPDM. In Sec. III, we apply the formalism to a two-band model to demonstrate its simulation capability and to analyze the transient optical conductivity and Kerr rotation under different pump-pulse conditions. In Sec. IV, we apply the formalism to a weakly spin-polarized germanium to demonstrate the capability of the formalism to tackle the complexity of a real material and of a realistic band structure. Finally, Sec. V summarizes our findings and discusses possible extensions of the present framework to more complex materials and correlated systems.

II. THEORY

A. The pumped system

Although this framework can be applied also to single atoms, molecules, photonic lattices, and many other kinds of systems, in this manuscript we focus on a lattice system driven by a linearly polarized electromagnetic pulse described by a vector potential $\boldsymbol{A}_{\rm pu}(t) = A_{\rm pu}(t)\hat{\boldsymbol{u}}_{\rm pu}$ and the corresponding electric field $\boldsymbol{E}_{\rm pu}(t) = E_{\rm pu}(t)\hat{\boldsymbol{u}}_{\rm pu} = -\partial_t A_{\rm pu}(t)\hat{\boldsymbol{u}}_{\rm pu}$, where $\hat{\boldsymbol{u}}_{\rm pu}$ identifies the polarization direction of the pump pulse. The pump pulse is assumed to act on the system starting from an initial time $t_{\rm ini} \to -\infty$. While we focus on linear pump polarization for simplicity in the following discussion, the formalism can be readily extended to account for a circularly polarized pump pulse.

In the dipole gauge, the time-dependent Hamiltonian of such a system takes the form [31,32,35]

$$\mathcal{H}(t) = \sum_{\mathbf{k},n,n'} c^\dagger_{\mathbf{k},n}(t)\Xi_{\mathbf{k},n,n'}(t)c_{\mathbf{k},n'}(t), \tag{1}$$

where $c_{\mathbf{k},n}(t)$ annihilates an electron with crystal momentum $\mathbf{k}$ and band index n; in the following, the index n will implicitly include the spin degree of freedom. The matrix $\Xi_{\mathbf{k}}(t)$ is obtained by the first-quantization single-particle Hamiltonian and reads as

$$\Xi_{\mathbf{k}}(t) = T_{\boldsymbol{k}}(t) + \mathrm{e}E_{\rm pu}(t)D_{\boldsymbol{k},\rm pu}(t), \tag{2}$$

where $D_{\boldsymbol{k},\rm pu}(t) = \boldsymbol{D}_{\boldsymbol{k}}(t)\cdot\hat{\boldsymbol{u}}_{\rm pu}$. Here, $T_{\boldsymbol{k}}(t)$ and $\boldsymbol{D}_{\boldsymbol{k}}(t)$ denote the time-dependent hopping and dipole matrices, respectively. They are constructed by applying the Peierls substitution in a localized basis (usually the Wannier basis) and then transforming to the band basis in which the equilibrium Hamiltonian is diagonal [31,32]. Hereafter, we distinguish operators written in the localized basis by an overscript $\sim$.

The transformation from the localized to the band basis is implemented via the unitary matrix $\Omega_{\mathbf{k}}$. In compact matrix notation, $\Omega^\dagger_{\mathbf{k}}\cdot\tilde{T}_{\mathbf{k}}\cdot\Omega_{\mathbf{k}}$ is diagonal, with the band energies $\varepsilon_{\mathbf{k},n}$ appearing on the diagonal. For a generic matrix M (representing any of T, $\boldsymbol{D}$, or their derivatives with respect to $\mathbf{k}$), we write

$$M_{\mathbf{k}}(t) = \Omega^\dagger_{\mathbf{k}}\cdot\tilde{M}_{\mathbf{k}+\frac{\mathrm{e}}{\hbar}\boldsymbol{A}_{\rm pu}(t)}\cdot\Omega_{\mathbf{k}}. \tag{3}$$

The symbol $\cdot$ is used to denote both vector products in Cartesian space and matrix products in the electronic Hilbert space. In realistic multiband systems, evaluated over dense $\mathbf{k}$ grids, it is computationally advantageous to expand $M_{\mathbf{k}+\frac{\mathrm{e}}{\hbar}\boldsymbol{A}_{\rm pu}(t)}$ in powers of the vector potential, by the so-called Peierls expansion [31].

Under the application of the pump pulse, DPOA allows us to express the time-evolved operators $c_{\mathbf{k}}(t)$ in the Heisenberg picture in terms of their equilibrium counterparts $c_{\mathbf{k}}(t_{\rm ini})$ [where $c_{\mathbf{k}}(t)$ denotes a column vector whose components are the operators $c_{\mathbf{k},n}(t)$]. This is achieved through the projection matrices $P_{\mathbf{k}}(t)$, such that

$$c_{\mathbf{k}}(t) = P_{\mathbf{k}}(t)\cdot c_{\mathbf{k}}(t_{\rm ini}). \tag{4}$$

The projection matrices satisfy the following equation of motion:

$$\mathrm{i}\hbar\partial_t P_{\mathbf{k}}(t) = \Xi_{\mathbf{k}}(t)\cdot P_{\mathbf{k}}(t), \tag{5}$$

which is solved numerically with the initial condition $P_{\mathbf{k}}(t_{\rm ini}) = \mathbf{1}$.

B. Transient optical conductivity

Besides the pump-pulse polarization $\hat{\boldsymbol{u}}_{\rm pu}$, we also introduce the incoming probe pulse polarization $\hat{\boldsymbol{u}}_{\rm in}$ and the outgoing probe pulse polarization $\hat{\boldsymbol{u}}_{\rm out}$. We also introduce a compact notation for the projection of vectors and rank-2 tensors in Cartesian space on unit vectors: $v_{\rm a} = \boldsymbol{v}\cdot\hat{\boldsymbol{u}}_{\rm a}$ and $s_{\rm a,b} = \hat{\boldsymbol{u}}_{\rm a}\cdot\boldsymbol{s}\cdot\hat{\boldsymbol{u}}_{\rm b}$, where a and b denote polarization directions such as pu, in, out, x, and y.

Within the generalized linear response theory [32], and by employing DPOA, the out-of-equilibrium two-time optical conductivity of a pumped system probed at time $t_{\rm pr}$ (the center of the probe pulse), $\sigma_{\rm out,in}(t, t_{\rm pr})$, can be written as [32]

$$\sigma_{\rm out,in}(t, t_{\rm pr}) = \sigma^{(1)}_{\rm out,in}(t, t_{\rm pr}) + \sigma^{(2)}_{\rm out,in}(t, t_{\rm pr}). \tag{6}$$

The first contribution reads as

$$\sigma^{(1)}_{\rm out,in}(t, t_{\rm pr}) = \frac{\mathrm{i}e}{\hbar\mathcal{V}}\theta(t - t_{\rm pr})\sum_{\boldsymbol{k}}\mathrm{Tr}\{Z_{\boldsymbol{k}}(t) \cdot [Y_{\boldsymbol{k}}(t) - Y_{\boldsymbol{k}}(t_{\rm pr}) + X_{\boldsymbol{k}}(t_{\rm pr})]\}, \tag{7}$$

where $\theta(t - t_{\rm pr})$ is the Heaviside theta function, $N_{\rm grid}$ is the number of points sampling the Brillouin zone (BZ), $e > 0$ is the electronic charge, and $\mathcal{V} = N_{\rm grid}v_{\rm uc}$ is the total system volume, in which $v_{\rm uc}$ is the unit-cell volume. The matrices $Z_{\boldsymbol{k}}(t)$, $Y_{\boldsymbol{k}}(t)$, and $X_{\boldsymbol{k}}(t)$ enable efficient numerical calculations and are defined as [32]

$$Z_{\boldsymbol{k}}(t) = (P^\dagger_{\boldsymbol{k}}(t)\cdot J_{\boldsymbol{k},\rm out}(t)\cdot P_{\boldsymbol{k}}(t))\circ\Delta F_{\boldsymbol{k}}, \tag{8}$$

$$Y_{\boldsymbol{k}}(t) = -\frac{e}{\hbar}\int_{t_{\rm ini}}^{t} dt' P^\dagger_{\boldsymbol{k}}(t')\cdot V_{\boldsymbol{k},\rm in}(t')\cdot P_{\boldsymbol{k}}(t'), \tag{9}$$

$$X_{\boldsymbol{k}}(t) = eP^\dagger_{\boldsymbol{k}}(t)\cdot D_{\boldsymbol{k},\rm in}(t)\cdot P_{\boldsymbol{k}}(t). \tag{10}$$

Here, $\Delta F_{\boldsymbol{k},n,n'} = f_{\boldsymbol{k},n} - f_{\boldsymbol{k},n'}$, with $f_{\boldsymbol{k},n} = \frac{1}{1+e^{-\beta(\varepsilon_{\boldsymbol{k},n}-\mu)}}$ the Fermi function, which determines the initial band occupations as the equilibrium thermal distribution, μ the chemical potential, and β the inverse temperature. The symbol $\circ$ denotes Hadamard (element-wise) matrix product. The current-related matrices are

$$J_{\boldsymbol{k},\mathrm{a}}(t) = \frac{1}{\hbar}\eta_{\boldsymbol{k},\mathrm{a}}(t) - \frac{\mathrm{i}}{\hbar}[D_{\boldsymbol{k},\mathrm{a}}(t), T_{\boldsymbol{k}}(t)], \tag{11}$$

$$\eta_{\boldsymbol{k},\mathrm{a}}(t) = \Omega^{\dagger}_{\boldsymbol{k}} \cdot \left(\hat{\boldsymbol{u}}_{\mathrm{a}} \cdot \nabla_{\boldsymbol{k}} \tilde{T}_{\boldsymbol{k}+\frac{e}{\hbar}\boldsymbol{A}_{\mathrm{pu}}(t)}\right) \cdot \Omega_{\boldsymbol{k}}, \tag{12}$$

$$V_{\boldsymbol{k},\mathrm{a}}(t) = \eta_{\boldsymbol{k},\mathrm{a}}(t) + e\Lambda_{\boldsymbol{k},\mathrm{a},\mathrm{pu}}(t)E_{\mathrm{pu}}(t), \tag{13}$$

$$\Lambda_{\boldsymbol{k},\mathrm{a},\mathrm{b}}(t) = \Omega^{\dagger}_{\boldsymbol{k}} \cdot \left(\hat{\boldsymbol{u}}_{\mathrm{a}} \cdot \nabla_{\boldsymbol{k}} \tilde{D}_{\boldsymbol{k}+\frac{e}{\hbar}\boldsymbol{A}_{\mathrm{pu}}(t),\mathrm{b}}\right) \cdot \Omega_{\boldsymbol{k}}, \tag{14}$$

where $[\Phi, \Psi]$ denotes the commutator.

The second contribution reads as

$$\sigma^{(2)}_{\mathrm{out,in}}(t, t_{\mathrm{pr}}) = \frac{e}{\mathcal{V}}\theta(t - t_{\mathrm{pr}}) \sum_{\boldsymbol{k}} \mathrm{Tr}\left\{\left(\frac{\delta J_{\boldsymbol{k}}}{\delta A}\right)_{\mathrm{out,in}}(t) \cdot \rho_{\boldsymbol{k}}(t)\right\}, \tag{15}$$

where $\rho_{\boldsymbol{k}}(t)$ is the SPDM:

$$\rho_{\boldsymbol{k},n,n'}(t) = \langle c^{\dagger}_{\boldsymbol{k},n'}(t) c_{\boldsymbol{k},n}(t)\rangle. \tag{16}$$

It can be readily shown that [31]

$$\rho_{\boldsymbol{k}}(t) = P_{\boldsymbol{k}}(t) \cdot F_{\boldsymbol{k}} \cdot P^{\dagger}_{\boldsymbol{k}}(t), \tag{17}$$

where $F_{\boldsymbol{k},n,n'} = \delta_{n,n'} f_{\boldsymbol{k},n}$. Furthermore,

$$\left(\frac{\delta J_{\boldsymbol{k}}}{\delta A}\right)_{\mathrm{out,in}}(t) = \frac{e}{\hbar^2}\xi_{\boldsymbol{k},\mathrm{out,in}}(t) - \frac{\mathrm{i}e}{\hbar^2}[\Lambda_{\boldsymbol{k},\mathrm{in,out}}(t), T_{\boldsymbol{k}}(t)] - \frac{\mathrm{i}e}{\hbar^2}[D_{\boldsymbol{k},\mathrm{out}}(t), \eta_{\boldsymbol{k},\mathrm{in}}(t)], \tag{18}$$

in which

$$\xi_{\boldsymbol{k},\mathrm{a},\mathrm{b}}(t) = \Omega^{\dagger}_{\boldsymbol{k}} \cdot \left[(\hat{\boldsymbol{u}}_{\mathrm{a}} \cdot \nabla_{\boldsymbol{k}})(\hat{\boldsymbol{u}}_{\mathrm{b}} \cdot \nabla_{\boldsymbol{k}})\tilde{T}_{\boldsymbol{k}+\frac{e}{\hbar}\boldsymbol{A}_{\mathrm{pu}}(t)}\right] \cdot \Omega_{\boldsymbol{k}}. \tag{19}$$

Once the full time-dependent optical conductivity $\sigma_{\mathrm{out,in}}(t, t_{\mathrm{pr}})$ is obtained, it is often more convenient to work in the frequency domain. This is done by performing a Fourier transform with respect to the relative time $t - t_{\mathrm{pr}}$, thus expressing the conductivity as a function of the probe pulse frequency ω:

$$\sigma_{\mathrm{out,in}}(\omega, t_{\mathrm{pr}}) = \int_{-\infty}^{+\infty} e^{\mathrm{i}(\omega+\mathrm{i}\lambda)(t-t_{\mathrm{pr}})}\sigma_{\mathrm{out,in}}(t, t_{\mathrm{pr}})dt, \tag{20}$$

where λ is a positive damping factor, which in some other works is dubbed 0^+. Since the optical conductivity is causal and thus proportional to the Heaviside function, the lower limit of the integral, $-\infty$, can be replaced by t_{pr}.

A substantial simplification in the numerical evaluation of Eq. (20) is obtained by observing that the pump pulse extends over a finite time interval. Specifically, one can restrict the upper limit of the integral to a cutoff time $t_{\mathrm{fin}} > t_{\mathrm{pr}}$, chosen such that the pump pulse has already become negligible, and rewrite

$$\sigma_{\mathrm{out,in}}(\omega, t_{\mathrm{pr}}) = \int_{-\infty}^{t_{\mathrm{fin}}} e^{\mathrm{i}(\omega+\mathrm{i}\lambda)(t-t_{\mathrm{pr}})}\sigma_{\mathrm{out,in}}(t, t_{\mathrm{pr}})dt + \sigma^{\mathrm{a.p.}}_{\mathrm{out,in}}(\omega, t_{\mathrm{fin}}, t_{\mathrm{pr}}), \tag{21}$$

where the second term, $\sigma^{\mathrm{a.p.}}_{\mathrm{out,in}}$, accounts for the contribution accumulated after the pump pulse has become negligible. This term naturally splits as

$$\sigma^{\mathrm{a.p.}}_{\mathrm{out,in}}(\omega, t_{\mathrm{fin}}, t_{\mathrm{pr}}) = \sigma^{(1),\mathrm{a.p.}}_{\mathrm{out,in}}(\omega, t_{\mathrm{fin}}, t_{\mathrm{pr}}) + \sigma^{(2),\mathrm{a.p.}}_{\mathrm{out,in}}(\omega, t_{\mathrm{fin}}, t_{\mathrm{pr}}), \tag{22}$$

and can be evaluated exploiting the fact that the Hamiltonian becomes stationary, once the pump pulse has become negligible, and reverts to its equilibrium form. One then obtains [33]

$$\sigma^{(1),\mathrm{a.p.}}_{\mathrm{out,in}}(\omega, t_{\mathrm{fin}}, t_{\mathrm{pr}}) = -\frac{\mathrm{i}e}{\hbar\mathcal{V}} e^{\mathrm{i}(\omega+\mathrm{i}\lambda)(t_{\mathrm{fin}}-t_{\mathrm{pr}})} \sum_{\boldsymbol{k}} \{W_{\boldsymbol{k}}(\omega, t_{\mathrm{fin}}) + \mathrm{Tr}[Q_{\boldsymbol{k}}(\omega, t_{\mathrm{fin}}) \cdot S_{\boldsymbol{k}}(t_{\mathrm{fin}}, t_{\mathrm{pr}})]\}, \tag{23}$$

where the auxiliary matrices read

$$Q_{\boldsymbol{k}}(\omega, t_{\mathrm{fin}}) = \mathrm{i}\{P^{\dagger}_{\boldsymbol{k}}(t_{\mathrm{fin}}) \cdot [J_{\boldsymbol{k},\mathrm{out}}(t_{\mathrm{fin}}) \circ \bar{w}_{\boldsymbol{k}}(\omega)] \cdot P_{\boldsymbol{k}}(t_{\mathrm{fin}})\} \circ \Delta F_{\boldsymbol{k}}, \tag{24}$$

$$S_{\boldsymbol{k}}(t_{\mathrm{fin}}, t_{\mathrm{pr}}) = -Y_{\boldsymbol{k}}(t_{\mathrm{fin}}) + Y_{\boldsymbol{k}}(t_{\mathrm{pr}}) - X_{\boldsymbol{k}}(t_{\mathrm{pr}}), \tag{25}$$

$$W_{\boldsymbol{k}}(\omega, t_{\mathrm{fin}}) = -\frac{e}{\hbar}\{\mathrm{Tr}[J_{\boldsymbol{k},\mathrm{out}}(t_{\mathrm{fin}}) \circ \bar{w}_{\boldsymbol{k}}(\omega)] \cdot [\eta_{\boldsymbol{k},\mathrm{in}}, \rho_{\boldsymbol{k}}(t_{\mathrm{fin}}) \circ \bar{w}^{\mathrm{T}}_{\boldsymbol{k}}(\omega)]\}, \tag{26}$$

with $\bar{w}_{\boldsymbol{k},n_1,n_2}(\omega) = \frac{1}{\omega+\omega_{\boldsymbol{k},n_1,n_2}+\mathrm{i}\lambda}$, $\omega_{\boldsymbol{k},n_1,n_2} = (\varepsilon_{\boldsymbol{k},n_1} - \varepsilon_{\boldsymbol{k},n_2})/\hbar$, and the superscript T denoting transposition. Similarly, one finds

$$\sigma^{(2),\mathrm{a.p.}}_{\mathrm{out,in}}(\omega, t_{\mathrm{fin}}, t_{\mathrm{pr}}) = \frac{e\mathrm{i}}{\mathcal{V}} e^{\mathrm{i}(\omega+\mathrm{i}\lambda)(t_{\mathrm{fin}}-t_{\mathrm{pr}})} \times \sum_{\boldsymbol{k}} \mathrm{Tr}\left\{\left(\left(\frac{\delta J_{\boldsymbol{k}}}{\delta A}\right)_{\mathrm{out,in}}(t_{\mathrm{fin}}) \circ \bar{w}_{\boldsymbol{k}}(\omega)\right).\rho_{\boldsymbol{k}}(t_{\mathrm{fin}})\right\}. \tag{27}$$

For the evaluation of these expressions, it is important to notice that both the hopping and dipole matrices, together with all their derivatives with respect to $\boldsymbol{k}$ [and hence also $J_{\boldsymbol{k},\mathrm{out}}$, $\eta_{\boldsymbol{k},\mathrm{in}}$, and $(\frac{\delta J_{\boldsymbol{k}}}{\delta A})_{\mathrm{out,in}}$], return to their equilibrium values at t_{fin}.

C. After-pump optical conductivity and dissipative effects

Once the pump pulse has become negligible, the Hamiltonian relaxes to its equilibrium form and becomes stationary. This fact enables a considerable simplification: the optical conductivity, which in general is a two-time function, can now be expressed solely in terms of the SPDM, which depends only on one time. Such a simplification is clearly not available if the probe pulse is applied while the pump pulse is still active, i.e., when t_{pr} lies within the pumping time interval. The stationary-Hamiltonian regime has already been addressed in the previous section: in Eq. (21), we reported the contribution accumulated after the pump pulse has become negligible.

To derive the post-pump optical conductivity, given that t_{pr} lies outside the pumping time interval, having the full SPDM, the Fourier transformation of the optical conductivity can be performed analytically and one can set $t_{\mathrm{fin}} = t_{\mathrm{pr}}$ in Eq. (21), which reduces to zero the first term on its right-hand side. Having set $t_{\mathrm{fin}} = t_{\mathrm{pr}}$ in Eqs. (23) and (27), and using the

identity $P_{\boldsymbol{k}}^{\dagger}(t) \cdot P_{\boldsymbol{k}}(t) = \mathbf{1}$, we arrive, after straightforward algebra, at (see Appendix A)

$$\sigma_{\text{out,in}}(\omega, t_{\text{pr}}) = \sigma^{(1)}_{\text{out,in}}(\omega, t_{\text{pr}}) + \sigma^{(2)}_{\text{out,in}}(\omega, t_{\text{pr}}), \tag{28}$$

with

$$\sigma^{(1)}_{\text{out,in}}(\omega, t_{\text{pr}}) = -\frac{\mathrm{i}e}{\hbar \mathcal{V}} \sum_{\boldsymbol{k}} \{W_{\boldsymbol{k}}(\omega, t_{\text{pr}}) + \mathrm{i}e\mathrm{Tr}([D_{\boldsymbol{k},\text{in}}(t_{\text{pr}}), J_{\boldsymbol{k},\text{out}}(t_{\text{pr}}) \circ \bar{w}_{\boldsymbol{k}}(\omega)] \cdot \rho_{\boldsymbol{k}}(t_{\text{pr}}))\}, \tag{29}$$

$$\sigma^{(2)}_{\text{out,in}}(\omega, t_{\text{pr}}) = \frac{\mathrm{i}e}{\mathcal{V}} \sum_{\boldsymbol{k}} \mathrm{Tr}\left\{ \left(\left(\frac{\delta J_{\boldsymbol{k}}}{\delta A} \right)_{\text{out,in}} (t_{\text{pr}}) \circ \bar{w}_{\boldsymbol{k}}(\omega) \right) \cdot \rho_{\boldsymbol{k}}(t_{\text{pr}}) \right\}. \tag{30}$$

An essential advantage of this formalism is that it allows one to consistently incorporate dissipative effects. In particular, one can add a phenomenological Markovian damping directly to the SPDM dynamics, thereby investigating its impact on the optical response. The essential requirement is that the damping timescale remains long compared to the oscillation period of the probe pulse ($\sim 2\pi/\omega$), so that the Hamiltonian remains effectively stationary. Considering that the decoherence and/or relaxation timescales are of the orders of several tens to hundreds of femtoseconds in many experimental setups (see Ref. [7] and the references therein), our phenomenological approach is valid in a wide range of cases.

The modified equation of motion for the SPDM then reads

$$\partial_t \rho_{\boldsymbol{k}}(t) = -\frac{\mathrm{i}}{\hbar}[\Xi_{\mathbf{k}}(t), \rho_{\boldsymbol{k}}(t)] - \Upsilon \circ (\rho_{\boldsymbol{k}}(t) - \rho_{\boldsymbol{k}}(t_{\text{ini}})), \tag{31}$$

where $\rho_{\boldsymbol{k}}(t_{\text{ini}}) = F_{\boldsymbol{k}}$ is the initial equilibrium distribution, and the matrix Υ encodes the phenomenological damping coefficients governing the relaxation processes.

In addition to enabling the straightforward incorporation of phenomenological damping, using SPDM in regimes where this is valid reduces computational cost relative to full DPOA calculations by a noticeable factor, which can reach an order of magnitude, depending on the final probe time. It is worth noting that the full DPOA calculations, in turn, are much more efficient (by one or even two orders of magnitude) than some other standard approaches, such as time dependent density functional theory (TD-DFT) calculations [7,31,32].

D. Magneto-optical Kerr rotation

The magneto-optical Kerr effect provides a powerful probe of symmetry breaking in solids, and is usually expressed in terms of the optical conductivity tensor, $\boldsymbol{\sigma}(\omega, t_{\text{pr}})$, or equivalently, the dielectric tensor, $\boldsymbol{\epsilon}(\omega, t_{\text{pr}})$. The latter is computed in terms of the former as [32]

$$\boldsymbol{\epsilon}(\omega, t_{\text{pr}}) = \mathbf{1} + \frac{\mathrm{i}}{\omega \epsilon_0} \boldsymbol{\sigma}(\omega, t_{\text{pr}}), \tag{32}$$

where ϵ_0 denotes the vacuum permittivity. In the simplest theoretical treatments, one evaluates the Kerr rotation angle from the longitudinal component σ_{xx}, together with the transverse component σ_{xy}, under the assumption that the latter is simply antisymmetric, i.e., $\sigma_{xy} = -\sigma_{yx}$, after the breakdown of time-reversal symmetry (TRS). Here, the x axis is chosen to be along the incoming probe pulse polarization, and the y axis is chosen in such a way that in a right-handed system the propagation direction of the incoming probe pulse is along $-z$. However, in more general situations—such as in crystals with linear birefringence—the transverse components of the optical conductivity may remain finite even in the absence of TRS breaking. In that case, they are symmetric rather than antisymmetric. To address this, we explicitly isolate the odd (antisymmetric) component of the transverse optical conductivity,

$$\sigma_{xy}^{\text{odd}} = \tfrac{1}{2}(\sigma_{xy} - \sigma_{yx}), \tag{33}$$

and employ this quantity to evaluate the Kerr response. For a probe pulse incident perpendicular to the sample surface, the magneto-optical (polar) Kerr rotation angle $\theta_K(\omega, t_{\text{pr}})$ is then obtained as [see Appendix B, and substitute Eq. (32) in Eq. (B50)]

$$\theta_K(\omega, t_{\text{pr}}) = \Re \frac{\sigma_{xy}^{\text{odd}}(\omega, t_{\text{pr}})}{\sigma_d(\omega, t_{\text{pr}}) \sqrt{1 + \frac{\mathrm{i}}{\omega \epsilon_0} \sigma_d(\omega, t_{\text{pr}})}}, \tag{34}$$

where $\sigma_d = \frac{1}{2}(\sigma_{xx} + \sigma_{yy})$.

III. TWO-BAND MODEL

In this section, we apply the formalism developed above to a minimal two-band model designed to capture the essential physics of pump-probe Kerr rotation angle dynamics in systems with SOC and broken TRS. This simplified model, which includes nearest-neighbor hopping, Rashba SOC, and Zeeman splitting, while not intended to reproduce the detailed electronic structure of a specific material, enables us to disentangle the microscopic mechanisms underlying the transient optical conductivity and the ensuing Kerr rotation. The results presented here illustrate the distinct features that emerge in and out of equilibrium and establish the connection between the microscopic electronic processes and experimentally measurable observables.

A. Model, computational details, and equilibrium optical response

The system consists of a two-orbital tight-binding model on a square lattice with lattice constant set to $a = 1\,\text{nm}$ for convenience. Each orbital accommodates two spin states, resulting in a total of four bands. The onsite energies and nearest-neighbor hoppings within a single-spin subspace are defined in the following.

We take the valence band (VB) and conduction band (CB) to originate from two localized Wannier states with onsite energies $\tilde{T}^{\text{hop}}_{\boldsymbol{R}=0,1,1} = -1.65\,\text{eV}$ and $\tilde{T}^{\text{hop}}_{\boldsymbol{R}=0,2,2} = 1.35\,\text{eV}$, respectively. The diagonal nearest-neighbor hoppings are

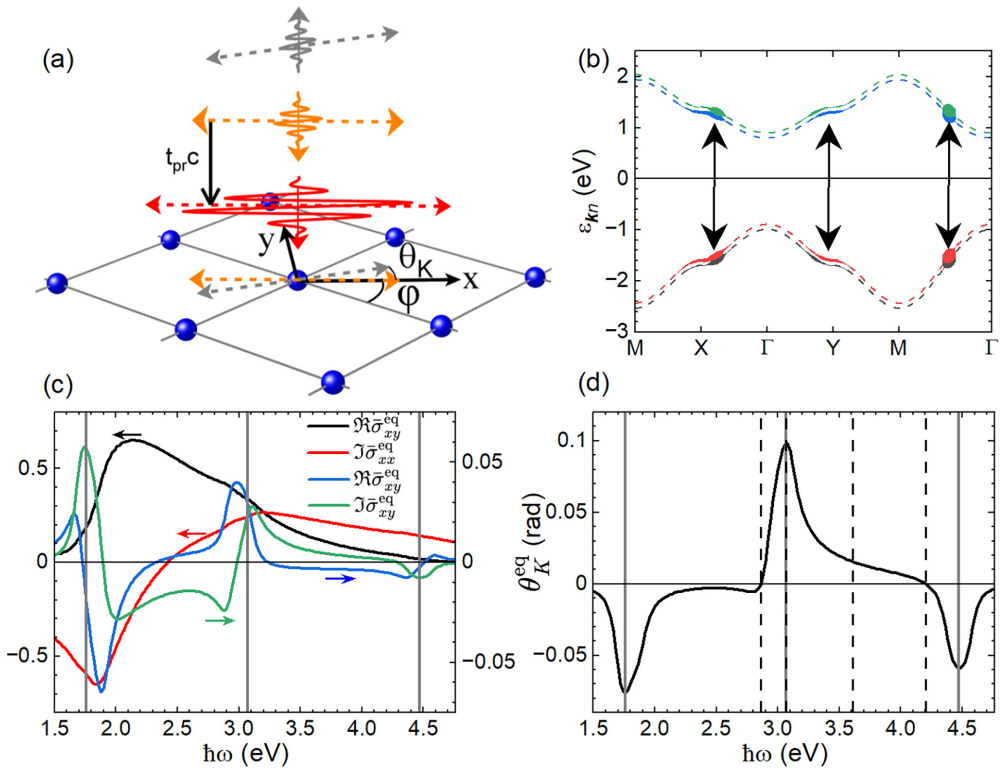


FIG. 1. (a) Schematic representation of the system, the pump pulse, and the time-delayed probe pulse together with its reflected component, showing the Kerr rotation of the reflected probe pulse polarization. The probe pulse arrives with a delay $t_{\rm pr}$ with respect to the pump pulse. The angle between the probe pulse polarization and the lattice vector is φ, which is set to $\varphi = 0$ in our calculations. (b) Band structure of the equilibrium Hamiltonian including Rashba SOC and Zeeman splitting. The thickness of the solid lines on top of the dashed lines indicates the postpump excitations, hole or electron, in VB or CB, respectively, for the pump-pulse photon energy of 2.86 eV. The double arrows mark the resonant interband energy gaps. (c) Real and imaginary parts of the equilibrium optical conductivities $\bar{\sigma}^{\rm eq}_{xx}(\omega)$ and $\bar{\sigma}^{\rm eq}_{xy}(\omega)$. Vertical gray solid lines mark the local extrema of $\theta^{\rm eq}_K(\omega)$, see (d). (d) Equilibrium Kerr rotation angle $\theta^{\rm eq}_K(\omega)$. Vertical gray lines correspond to the local extrema of $\theta^{\rm eq}_K(\omega)$, and vertical dashed lines indicate the pump photon energies used in the time-dependent simulations.

$\tilde{T}^{\rm hop}_{\mathbf{R}=\mathbf{a},1,1} = 0.2\,\text{eV}$ and $\tilde{T}^{\rm hop}_{\mathbf{R}=\mathbf{a},2,2} = -0.15\,\text{eV}$, while the off-diagonal hoppings are $\tilde{T}^{\rm hop}_{\mathbf{R}=\mathbf{a},1,2} = \tilde{T}^{\rm hop}_{\mathbf{R}=\mathbf{a},2,1} = -0.1\,\text{eV}$. Here, $\tilde{T}^{\rm hop}_{\boldsymbol{R},\nu,\nu'}$ denotes the hopping matrix between two Wannier states ν and ν' centered at sites separated by $\boldsymbol{R}$, and $\mathbf{a} \in \{a(\pm1, 0), a(0, \pm1)\}$. For bulk calculations, the BZ is sampled as a 128×128 $\boldsymbol{k}$-grid centered at Γ. The damping factor used in evaluating the optical conductivity is set to $\lambda = 0.1$ PHz. Fourier transforming $\tilde{T}^{\rm hop}_{\boldsymbol{R}}$ yields the momentum-space hopping matrix $\tilde{T}^{\rm hop}_{\boldsymbol{k}}$ [31,32].

This minimal model allows us to explore generic phenomena that can arise in realistic pump-probe experiments while avoiding complications related to material-specific details. The underlying formalism, however, remains general and can be applied to any lattice structure or multiband systems.

A key ingredient for the emergence of Kerr rotation is the presence of SOC. We include a Rashba SOC term of the form

$$\tilde{T}^{\rm Rashba}_{\boldsymbol{k}} = \alpha_{\rm Rashba}\left[\sin(k_x a)\varsigma^{\rm spin}_y - \sin(k_y a)\varsigma^{\rm spin}_x\right] \otimes \varsigma^{\rm orb}_y, \tag{35}$$

where $\varsigma^{\rm spin/orb}_{x/y}$ are the Pauli matrices acting on the spin and orbital subspaces, respectively, and we set $\alpha_{\rm Rashba} = 0.1\,\text{eV}$. The Rashba term alone preserves TRS. To break TRS, we include a Zeeman term

$$\tilde{T}^{\rm Zeeman}_{\boldsymbol{k}} = \alpha_{\rm Zeeman}\varsigma^{\rm spin}_z, \tag{36}$$

with $\alpha_{\rm Zeeman} = 0.05\,\text{eV}$. The total equilibrium Hamiltonian in the localized Wannier basis is therefore given by

$$\tilde{T}_{\boldsymbol{k}} = \tilde{T}^{\rm hop}_{\boldsymbol{k}} + \tilde{T}^{\rm Rashba}_{\boldsymbol{k}} + \tilde{T}^{\rm Zeeman}_{\boldsymbol{k}}. \tag{37}$$

We set the chemical potential and the temperature to zero. As such, we have two VBs and two CBs.

We simulate a pump-probe experiment where the system is driven by a linearly polarized pump pulse described by a vector potential $\boldsymbol{A}_{\rm pu}(t) = A_{\rm pu}(t)\hat{\boldsymbol{u}}_{\rm pu}$, with

$$A_{\rm pu}(t) = A_0 e^{-(4\ln 2)t^2/\tau^2_{\rm pu}} \sin(\omega_{\rm pu} t), \tag{38}$$

where $\tau_{\rm pu}$ is the FWHM of the pulse envelope. We set $\tau_{\rm pu} = 10$ fs and the pump-pulse amplitude $A_0 = 0.5\,\text{V/nm fs}$. A time-delayed probe pulse is applied with polarization $\hat{\boldsymbol{u}}_{\rm in} = \hat{\boldsymbol{u}}_{\rm pu} = \hat{x}$. The polarization of the reflected probe pulse is changed by the Kerr rotation angle $\theta_K(\omega, t_{\rm pr})$.

Figure 1(a) schematically shows the overall geometry of the system, the incident pump and probe pulses, and the Kerr rotation of the reflected probe pulse.

Postpump excitations occur mainly at $\boldsymbol{k}$ points where the interband gap matches the pump photon energy

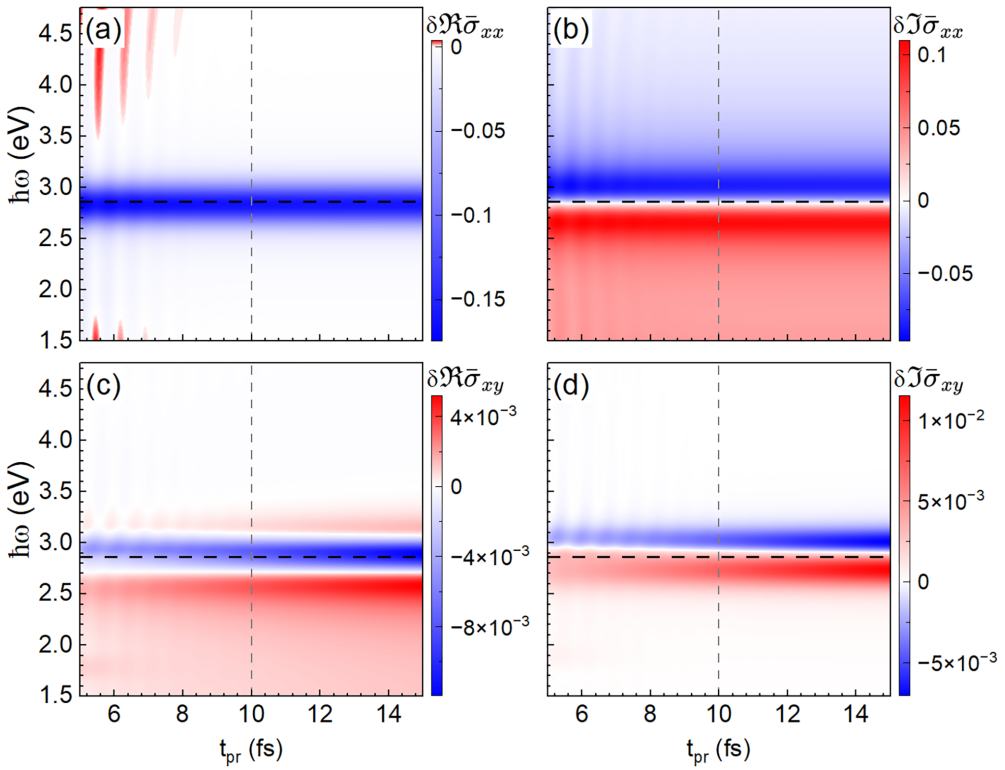


FIG. 2. (a)–(d) Real and imaginary parts of $\delta\bar{\sigma}_{xx}(\omega, t_{\rm pr})$ and $\delta\bar{\sigma}_{xy}(\omega, t_{\rm pr})$ as functions of ω and $t_{\rm pr}$. The horizontal dashed lines mark the pump-pulse frequency $\hbar\omega_{\rm pu} = 2.86\,\text{eV}$, while the vertical dashed lines indicate the probe pulse delay equal to the pump-pulse FWHM, $t_{\rm pr} = \tau_{\rm pu} = 10\,\text{fs}$.

$\hbar\omega_{\rm pu} = 2.86\,\text{eV}$, as shown in Fig. 1(b), on top of the system bands along a specific path in the BZ. Along the Γ–Y path, small excitations also appear due to SOC, which couples spin and orbital degrees of freedom. Without SOC, no excitations would occur there for the chosen pump polarization, because $\eta_{\boldsymbol{k},x} = 0$ for the $\boldsymbol{k}$ points along Γ–Y for this model [31].

When the probe pulse arrives well before the pump pulse (equivalently, when no pump pulse is applied), the optical response corresponds to the equilibrium case, and is denoted by the superscript "eq" (the expression for the analytical equilibrium optical conductivity is reported in Refs. [32,33]). For plotting convenience, all optical conductivities are reported in the figures in a dimensionless form $\bar{\sigma} = \sigma/(\omega\epsilon_0)$. The equilibrium components $\bar{\sigma}^{\rm eq}_{xx}(\omega)$ and $\bar{\sigma}^{\rm eq}_{xy}(\omega)$ are shown in Fig. 1(c). The real part, $\Re\bar{\sigma}^{\rm eq}_{xx}$, is related to absorption and decreases outside the band-gap regions. The real and imaginary parts of $\bar{\sigma}$ are related through the Kramers-Kronig (KK) relations, implying that local extrema in one correspond to dispersive features in the other. We dub such features as KK counterparts.

The equilibrium Kerr rotation angle $\theta^{\rm eq}_K(\omega)$, shown in Fig. 1(d), exhibits local extrema around the same frequencies where the KK-counterpart features appear in $\Re\bar{\sigma}^{\rm eq}_{xy}(\omega)$ and $\Im\bar{\sigma}^{\rm eq}_{xy}(\omega)$. However, the dominant feature cannot be inferred *a priori* due to the nonlinear dependence of the Kerr rotation on the optical conductivity tensor, see Eq. (34). The vertical dashed lines indicate the four pump-pulse frequencies considered in the following simulations, one of which coincides with a local maximum in $\theta^{\rm eq}_K(\omega)$. Unless otherwise specified, the pump-pulse frequency for the toy model is $\hbar\omega_{\rm pu} = 2.86\,\text{eV}$, the frequency at which we have $\theta^{\rm eq}_K(\omega_{\rm pu}) = 0$.

B. Transient optical conductivity and Kerr rotation

Figure 2 shows the temporal evolution of the changes in optical conductivity, $\delta\bar{\sigma}_{\alpha\beta}(\omega, t_{\rm pr}) = \bar{\sigma}_{\alpha\beta}(\omega, t_{\rm pr}) - \bar{\sigma}^{\rm eq}_{\alpha\beta}(\omega)$, which is dubbed differential optical conductivity. During the pump-pulse application ($t_{\rm pr} \lesssim \tau_{\rm pu}$), both real and imaginary parts exhibit rapid oscillations with frequency $\sim 2\omega_{\rm pu}$. After pumping the system ($t_{\rm pr} \gg \tau_{\rm pu}$), these fast oscillations disappear and the real parts of the differential optical conductivities remain negative near the resonant frequency $\omega \approx \omega_{\rm pu}$ [the blue stripes in Figs. 2(a) and 2(c)]. This behavior reflects a reduction in absorption caused by photoexcited carriers that block further probe-induced interband transitions, the so-called Pauli blocking [32], which is also dubbed state blocking [36,37]. The imaginary parts of the optical conductivities display KK-counterpart features relative to their real parts.

The evolution of the Kerr rotation, $\delta\theta_K(\omega, t_{\rm pr}) = \theta_K(\omega, t_{\rm pr}) - \theta^{\rm eq}_K(\omega)$, for four distinct pump-pulse frequencies is presented in Fig. 3. During the pump-pulse time interval ($t_{\rm pr} \lesssim \tau_{\rm pu}$), $\delta\theta_K$ exhibits fast oscillations. These fast oscillations vanish when the pump pulse becomes negligible ($t_{\rm pr} \gg \tau_{\rm pu}$). Near-resonant features appear around $\omega \approx \omega_{\rm pu}$, resembling those in Fig. 2. The detailed form of these near-resonant features—whether stripe-like [as in Figs. 3(a) and 3(b)] or its KK counterpart [as in Figs. 3(c) and 3(d)]—depends on the complex interplay of real and imaginary parts of σ_{xx} and σ_{xy} in Eq. (34), and therefore is different for different pump-pulse frequencies.

Interestingly, additional features emerge at the frequencies where the equilibrium Kerr rotation exhibits local extrema [vertical gray lines in Fig. 1(d)]. This can be understood by

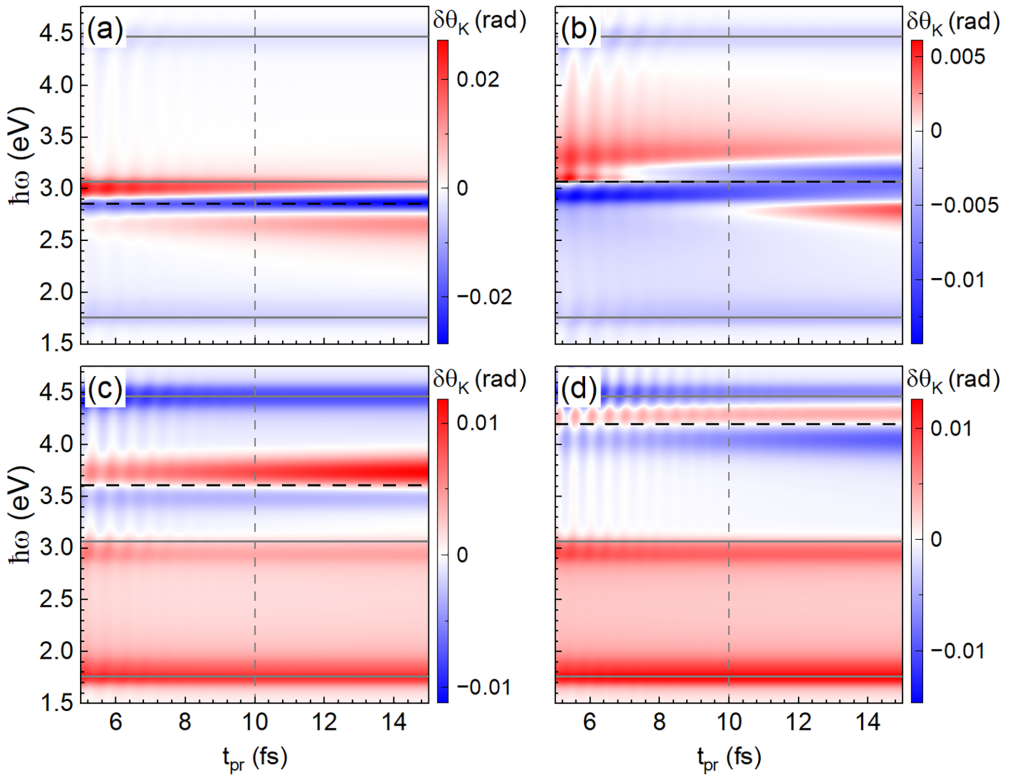


FIG. 3. (a)–(d) The evolution of the Kerr rotation angle $\delta\theta_K(\omega, t_{\rm pr})$ for four different pump-pulse frequencies indicated in Fig. 1(d). Horizontal dashed lines correspond to the respective pump-pulse frequencies. Horizontal gray lines correspond to the local extrema of $\theta_K^{\rm eq}(\omega)$, see Fig. 1(d).

considering a simplified ratio $f(\omega) = g(\omega)/h(\omega)$ that mimics the Kerr functional dependence. Upon pumping, $g \to g^{\rm eq} + \delta g$ and $h \to h^{\rm eq} + \delta h$, which results in a variation, $f \to f^{\rm eq} + \delta f$, which up to the first order reads $\delta f = \delta g/h^{\rm eq} - (\delta h/h^{\rm eq}) f^{\rm eq}$. Thus, even when δg and δh are small off resonance, the product with $f^{\rm eq}$ produces additional structures at its local extrema.

C. Long-time dynamics and damping effects

In many experiments, the long-delay regime ($t_{\rm pr} \gg \tau_{\rm pu}$) of the Kerr response is of particular interest. Calculations in such regime become computationally more feasible within the SPDM framework, which, as discussed in Sec. II C, is valid only after the pump pulse has become negligible. Figure 4(a) benchmarks the exact $\delta\theta_K$ results against SPDM simulations without damping [$\Upsilon = 0$ in Eq. (31)]. The agreement improves systematically as $t_{\rm pr}$ exceeds the pump-pulse duration, confirming the applicability of the SPDM approach.

Figure 4(b) displays $\delta\theta_K(\omega, t_{\rm pr})$ for long delays without damping. A slow oscillation in time appears, whose frequency corresponds to $\frac{2\pi\hbar}{2\alpha_{\rm Zeeman}}$. This beating pattern originates from the interference between off-diagonal SPDM elements $\rho_{\boldsymbol{k}nm}(t)$ (the *coherences*) oscillating with slightly different interband energy gaps, which in our case comes from the Zeeman splitting. In real materials, similar beating effects are expected due to small band splittings caused by SOC, spin polarization, Zeeman terms, etc.

Finally, Fig. 4(c) shows the impact of damping, implemented phenomenologically in SPDM via $\Upsilon_{nm} = \delta_{nm}\frac{\lambda}{4} + (1 - \delta_{nm})\frac{\lambda}{2}$, where off-diagonal elements decay faster than the diagonal ones [38]. Damping reduces the overall amplitude of the Kerr rotation angle and gradually suppresses oscillations as $t_{\rm pr}$ increases.

IV. WEAKLY SPIN-POLARIZED GERMANIUM

In this section, we present our results for weakly spin-polarized germanium, illustrating the capability of the framework to compute the Kerr rotation in a real material while accounting for all the difficulties and complexities associated with a realistic band structure.

A. Weakly spin-polarized germanium and pump-probe setup

We consider weakly spin-polarized germanium (magnetic moment per cell $\approx 6 \times 10^{-5}\,\mu_{\rm B}$) to break TRS and enable the measurement of a finite Kerr rotation in a material that intrinsically possesses finite SOC. The spin polarization can be in principle achieved experimentally through standard methods, such as exploiting proximity effects [39]. The band structure was obtained with the elk code [40] in the presence of an *ad hoc* magnetic field, and the hopping parameters ($\tilde{T}_{\mathbf{k}}$) and dipole matrix elements ($\tilde{\mathbf{D}}_{\mathbf{k}}$) were computed using the wannier90 code [41], as in Ref. [7]. We focused on the closed manifold of 16 sp^3 bands surrounding the chemical potential, which lies within the main band gap of $\approx$800 meV.

In this case, we simulate the pump-probe experiment with a pump-pulse vector potential characterized by a FWHM $\tau_{\rm pu} = 10$ fs, amplitude $A_0 = 0.5276\,{\rm V/nm\,fs}$, and frequency

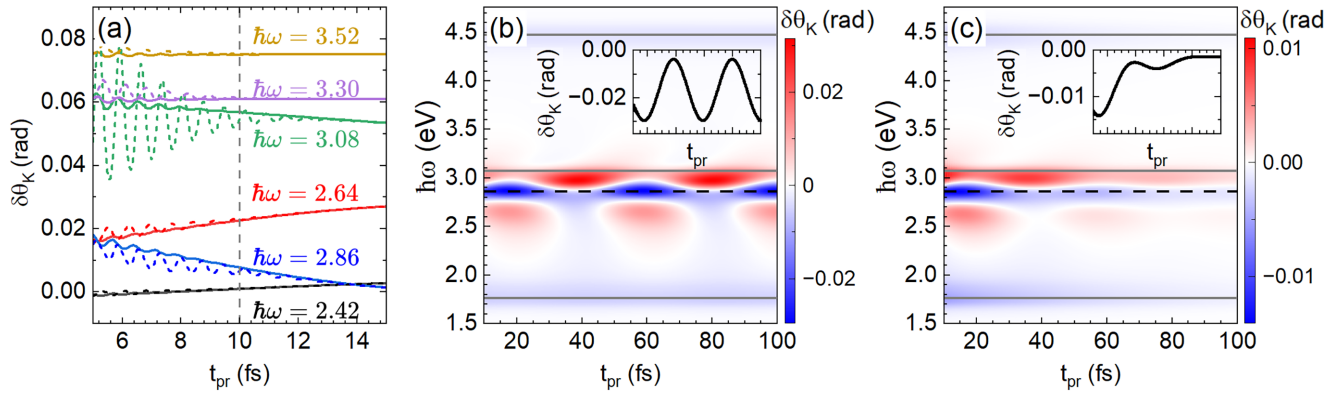


FIG. 4. (a) Benchmark of the exact results for $\delta\theta_K(\omega, t_{\rm pr})$ against those obtained from the SPDM approach without damping [$\Upsilon = 0$ in Eq. (31)] for several probe pulse frequency cuts. The probe photon energy values of each cut, $\hbar\omega$, are given in electron volts. An offset of 0.015 rad has been applied on increasing the probe photon energies. The pump photon energy is $\hbar\omega_{\rm pu} = 2.86$ eV. (b) $\delta\theta_K(\omega, t_{\rm pr})$ at long delays without damping; the inset shows a cut at the resonant frequency $\omega = \omega_{\rm pu}$. (c) Same as (b) but including damping in SPDM with $\Upsilon_{nm} = \delta_{nm}\frac{\lambda}{4} + (1 - \delta_{nm})\frac{\lambda}{2}$. The horizontal solid and dashed lines in (b) and (c) are the same as those in Fig. 3(a).

$\hbar\omega_{\rm pu} = 1.55$ eV. We explore the frequency spectrum within the near-infrared and visible region with the probe, revealing transitions up to a few multiphoton resonances of the pump-pulse frequency between valence and conduction bands. The crystal orientation is the same as in Ref. [7], and both the pump and probe polarizations are along the direction [1 0 0]. The BZ is sampled on a $32 \times 32 \times 32$ $\boldsymbol{k}$ grid centered at Γ, and the damping factor is set to $\lambda = 0.25$ PHz.

B. Kerr rotation: Equilibrium, long-time dynamics, and damping effects

In Fig. 5, we report the Kerr rotation angle $\theta_K(\omega)$ as a function of the probe frequency, computed for our realization of weakly spin-polarized germanium. Figure 5(a) shows the equilibrium Kerr rotation angle $\theta_K^{\rm eq}(\omega)$ in the near-infrared and visible frequency ranges. The complexity of the band structure of a real material is reflected in the rich frequency dependence of the Kerr-rotation features.

Figure 5(b) displays the differential Kerr rotation $\delta\theta_K(\omega, t_{\rm pr}) = \theta_K(\omega, t_{\rm pr}) - \theta_K^{\rm eq}(\omega)$ as a function of the probe frequency and delay time, in the long-delay (postpump) regime with the undamped dynamics, i.e., with $\Upsilon = 0$. The inset shows a cut at the two-photon resonant frequency $\omega = 2\omega_{\rm pu}$, where the maximum variation occurs. This behavior is consistent with Ref. [7], where two-photon processes were found to play the dominant role in inducing charge accumulation in the postpump regime. Moreover, this analysis clearly demonstrates that the Kerr rotation angle can be used experimentally to identify the relevant n-photon resonances for a given material. The signals expected at the local extrema of the equilibrium Kerr rotation are barely visible, or even invisible, on the scale of the main signal, which is much larger in amplitude. The fast oscillations follow approximately twice the pump frequency and originate from the interference of off-diagonal (coherence) terms of the single-particle density matrix among $\boldsymbol{k}$ points in the valence and conduction bands at different multiphoton resonances. Such $\boldsymbol{k}$ points host post-pump electronic excitations. It is worth noting that, for this

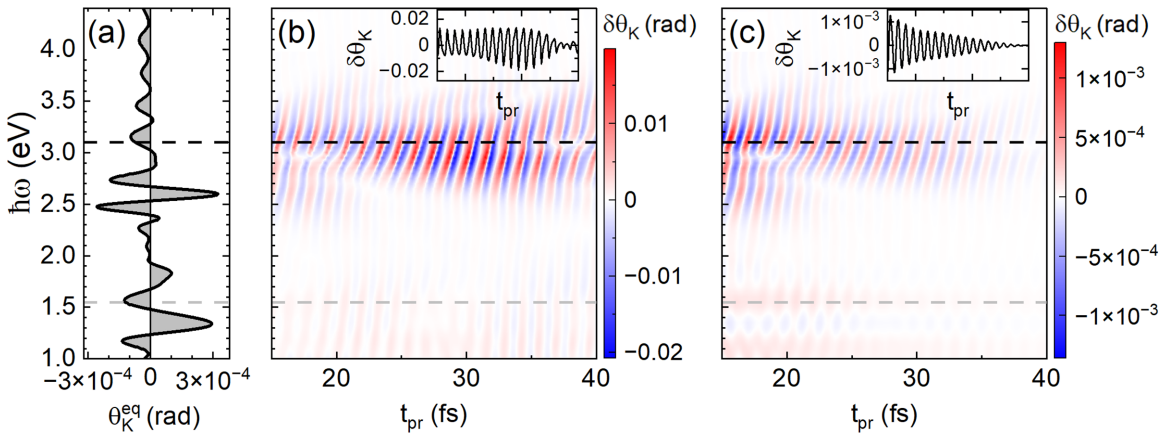


FIG. 5. (a) Equilibrium Kerr rotation $\theta_K^{\rm eq}(\omega)$ of weakly spin-polarized germanium. (b) $\delta\theta_K(\omega, t_{\rm pr})$ at long delays without damping; the inset shows a cut at the two-photon resonant frequency $\omega = 2\omega_{\rm pu}$. (c) Same as (b) but including damping in SPDM with $\Upsilon_{nm} = \delta_{nm}\frac{\lambda}{4} + (1 - \delta_{nm})\frac{\lambda}{2}$. The horizontal gray and black dashed lines in all panels mark the one- and two-photon resonances, $\hbar\omega = \hbar\omega_{\rm pu} = 1.55$ eV and $\hbar\omega = 2\hbar\omega_{\rm pu} = 3.10$ eV, respectively.

system, several distinct multiphoton resonances can coexist at the same $\boldsymbol{k}$ point. The slow beating instead follows the energy splitting induced by the spin polarization.

Figure 5(c) shows the differential Kerr rotation $\delta\theta_K(\omega, t_{\rm pr})$ computed for the same parameters as in Fig. 5(a), except that the damping $\Upsilon_{nm} = \delta_{nm}\frac{\lambda}{4} + (1-\delta_{nm})\frac{\lambda}{2}$ is included. In this case, the expected signal at the local extrema of the equilibrium Kerr rotation becomes clearly visible, at least for the most pronounced ones. Furthermore, the beating behavior disappears because the damping acts on a shorter timescale.

V. CONCLUSIONS AND PERSPECTIVE

We have developed a general and efficient theoretical framework for computing the time-resolved magneto-optical Kerr effect in ultrafast pump-probe experiments. Our approach, based on the DPOA, provides a direct link between the microscopic nonequilibrium dynamics of a photoexcited system and its macroscopic magneto-optical response. This formulation offers a transparent physical picture and significant numerical advantages, being fully general for multiband systems with arbitrary lattice structures, spin-orbit coupling, and symmetry breaking.

We presented a derivation of a simplified expression for the optical conductivity that is valid after the pump pulse has become negligible, which depends solely on the SPDM at the probe pulse time. This postpump simplification drastically reduces the computational cost for studying long-time dynamics. Furthermore, the framework naturally allows for the inclusion of phenomenological damping within the SPDM dynamics, enabling the modeling of essential relaxation processes that dominate the experimental postpump regime.

We illustrated the applicability of this formalism by applying it to a minimal two-band model. The numerical results successfully capture the hallmark features of the ultrafast magneto-optical Kerr effect, including the rapid, pump-induced oscillations during the excitation and the emergence of persistent spectral features near the pump-pulse frequency after the pulse application, such as reduced absorption due to Pauli blocking. The calculated Kerr rotation also reveals additional structures at the equilibrium local extrema positions, arising from the nonlinear dependence of the Kerr angle on the conductivity tensor, as well as long-time beating patterns originating from quantum interference between different interband coherences.

The application to a realization of weakly spin-polarized germanium instead proved the capability of the formalism to handle even the complex band structures of real materials and that the Kerr rotation can be used to deduct experimentally the relevant n-photon resonances for a given specific material.

The presented framework is readily extendable to more complex materials—such as altermagnets and topological insulators—where the interplay of light, spin, orbital, and charge degrees of freedom leads to rich, nonequilibrium physics. By bridging microscopic dynamics and experimental observables, our theory provides a powerful tool for interpreting and guiding future time-resolved magneto-optical studies across a wide range of quantum materials.

ACKNOWLEDGMENTS

The authors thank Jeroen van den Brink for insightful discussions. The authors acknowledge support by MUR under Project PNRR MUR Missione 4 (SPOKE 2) TOPQIN "TOPological Qubit In driveN and reconfigurable heterostructures."

DATA AVAILABILITY

The data that support the findings of this article are openly available [42].

APPENDIX A: DERIVATION OF EQ. (29)

In this Appendix, we derive Eq. (29). Setting $t_{\rm fin} = t_{\rm pr}$ in Eq. (23), we obtain $\sigma^{(1),\rm a.p.}_{\rm out,in}(\omega, t_{\rm fin}, t_{\rm pr}) \to \sigma^{(1)}_{\rm out,in}(\omega, t_{\rm pr})$, where

$$\sigma^{(1)}_{\rm out,in}(\omega, t_{\rm pr}) = -\frac{ie}{\hbar\mathcal{V}}\sum_{\boldsymbol{k}}\{W_{\boldsymbol{k}}(\omega, t_{\rm pr}) + {\rm Tr}[Q_{\boldsymbol{k}}(\omega, t_{\rm pr})\cdot S_{\boldsymbol{k}}(t_{\rm pr}, t_{\rm pr})]\}. \tag{A1}$$

Using Eqs. (24), (25), and (10), we have

$${\rm Tr}[Q_{\boldsymbol{k}}(\omega, t_{\rm pr})\cdot S_{\boldsymbol{k}}(t_{\rm pr}, t_{\rm pr})] = -ei\sum_{n,n'}\left(\left\{P^\dagger_{\boldsymbol{k}}(t_{\rm pr})\cdot J^{\bar{w}}_{\boldsymbol{k},\rm out}(\omega, t_{\rm pr})\cdot P_{\boldsymbol{k}}(t_{\rm pr})\right\}\circ\Delta F_{\boldsymbol{k}}\right)_{nn'}(P^\dagger_{\boldsymbol{k}}(t_{\rm pr})\cdot D_{\boldsymbol{k},\rm in}(t_{\rm pr})\cdot P_{\boldsymbol{k}}(t_{\rm pr}))_{n'n}, \tag{A2}$$

where, for the sake of simplicity, we have defined $J^{\bar{w}}_{\boldsymbol{k},\rm out}(\omega, t_{\rm pr}) = J_{\boldsymbol{k},\rm out}(t_{\rm pr})\circ\bar{w}_{\boldsymbol{k}}(\omega)$. Using $\Delta F_{\boldsymbol{k},nn'} = f_{\boldsymbol{k},n} - f_{\boldsymbol{k},n'}$, we get

$$\begin{aligned}{\rm Tr}[Q_{\boldsymbol{k}}(\omega, t_{\rm pr})\cdot S_{\boldsymbol{k}}(t_{\rm pr}, t_{\rm pr})] =& -ei\sum_{n,n'}\Big\{\left\{P^\dagger_{\boldsymbol{k}}(t_{\rm pr})\cdot J^{\bar{w}}_{\boldsymbol{k},\rm out}(\omega, t_{\rm pr})\cdot P_{\boldsymbol{k}}(t_{\rm pr})\right\}_{nn'} f_{\boldsymbol{k},n}(P^\dagger_{\boldsymbol{k}}(t_{\rm pr})\cdot D_{\boldsymbol{k},\rm in}(t_{\rm pr})\cdot P_{\boldsymbol{k}}(t_{\rm pr}))_{n'n}\\ &- \left\{P^\dagger_{\boldsymbol{k}}(t_{\rm pr})\cdot J^{\bar{w}}_{\boldsymbol{k},\rm out}(\omega, t_{\rm pr})\cdot P_{\boldsymbol{k}}(t_{\rm pr})\right\}_{nn'} f_{\boldsymbol{k},n'}(P^\dagger_{\boldsymbol{k}}(t_{\rm pr})\cdot D_{\boldsymbol{k},\rm in}(t_{\rm pr})\cdot P_{\boldsymbol{k}}(t_{\rm pr}))_{n'n}\Big\},\end{aligned} \tag{A3}$$

which can be written in the following compact form:

$$\begin{aligned}{\rm Tr}[Q_{\boldsymbol{k}}(\omega, t_{\rm pr})\cdot S_{\boldsymbol{k}}(t_{\rm pr}, t_{\rm pr})] =& -ei{\rm Tr}\Big\{F_{\boldsymbol{k}}\cdot P^\dagger_{\boldsymbol{k}}(t_{\rm pr})\cdot J^{\bar{w}}_{\boldsymbol{k},\rm out}(\omega, t_{\rm pr})\cdot P_{\boldsymbol{k}}(t_{\rm pr})\cdot P^\dagger_{\boldsymbol{k}}(t_{\rm pr})\cdot D_{\boldsymbol{k},\rm in}(t_{\rm pr})\cdot P_{\boldsymbol{k}}(t_{\rm pr})\\ &- P^\dagger_{\boldsymbol{k}}(t_{\rm pr})\cdot J^{\bar{w}}_{\boldsymbol{k},\rm out}(\omega, t_{\rm pr})\cdot P_{\boldsymbol{k}}(t_{\rm pr})\cdot F_{\boldsymbol{k}}\cdot P^\dagger_{\boldsymbol{k}}(t_{\rm pr})\cdot D_{\boldsymbol{k},\rm in}(t_{\rm pr})\cdot P_{\boldsymbol{k}}(t_{\rm pr})\Big\}.\end{aligned} \tag{A4}$$

Using the cyclic property of trace, Eq. (17), and $P^\dagger_{\boldsymbol{k}}(t)\cdot P_{\boldsymbol{k}}(t) = \mathbf{1}$, we obtain

$${\rm Tr}[Q_{\boldsymbol{k}}(\omega, t_{\rm pr})\cdot S_{\boldsymbol{k}}(t_{\rm pr}, t_{\rm pr})] = ei{\rm Tr}\left\{\left[D_{\boldsymbol{k},\rm in}(t_{\rm pr}), J^{\bar{w}}_{\boldsymbol{k},\rm out}(\omega, t_{\rm pr})\right]\cdot\rho_{\boldsymbol{k}}(t_{\rm pr})\right\}. \tag{A5}$$

Substituting back in Eq. (A1), one obtains Eq. (29), given in the main text.

It is worth noting that unlike Eqs. (29) and (30) does not need a detailed derivation, as by setting $t_{\text{fin}} = t_{\text{pr}}$ in Eq. (27), one immediately obtains it.

APPENDIX B: COMPUTING POLAR KERR ROTATION ANGLE FROM THE DIELECTRIC TENSOR

Let us consider a monochromatic electromagnetic plane wave impinging perpendicularly on the surface, lying in the xy plane, of a neutral (zero free charge density) dielectric (zero free current density) optically linear sample in the polar Kerr geometry (magneto-optic medium with magnetization along axis z) with a possible nonmagnetic optical anisotropy only in the xy plane,

$$\mathbf{E}^a_\omega(\mathbf{r},t) = \mathbf{E}^a_0(\omega)\mathrm{e}^{\mathrm{i}\frac{\omega}{c}[\mathbf{n}_a(\omega)\cdot\mathbf{r}-ct]} \tag{B1}$$

$$\mathbf{E}^a_0(\omega) = \left(E^a_{0x}(\omega), E^a_{0y}(\omega), E^a_{0z}(\omega)\right) \tag{B2}$$

$$\mathbf{n}_a(\omega) = [0,0,n_a(\omega)], \tag{B3}$$

where $\mathbf{E}^a_\omega(\mathbf{r},t)$ is the electric field; $a = i,\ i',\ r$ stands for incident, reflected, and refracted wave, respectively; and $n_a(\omega) = -1\ (i),\ 1\ (i'),\ -n(\omega)\ (r)$ is the (generally complex) refractive index of the traversed medium, respectively. $\mathbf{n}_a(\omega)$ has only the z component for all three waves because of the kinematic conservation of the momentum parallel to the interface (Snell law for flat, homogeneous, and static interface in linear optics) [43–46]. Normal incidence gives $E^i_{0z}(\omega) = 0$.

The relevant Maxwell's equations read as

$$\nabla\cdot\mathbf{D}^a_\omega(\mathbf{r},t) = 0 \Rightarrow \mathbf{n}_a(\omega)\cdot\mathbf{D}^a_0(\omega) = 0 \tag{B4}$$

$$\nabla\times\mathbf{E}^a_\omega(\mathbf{r},t) = -\frac{\partial\mathbf{B}^a_\omega}{\partial t}(\mathbf{r},t) \tag{B5}$$

$$\nabla\times\mathbf{B}^a_\omega(\mathbf{r},t) = \mu_0\frac{\partial\mathbf{D}^a_\omega}{\partial t}(\mathbf{r},t), \tag{B6}$$

where $\mathbf{D}^a_\omega(\mathbf{r},t) = \mathbf{D}^a_0(\omega)\mathrm{e}^{\mathrm{i}\frac{\omega}{c}[\mathbf{n}_a(\omega)\cdot\mathbf{r}-ct]}$ is the electric displacement field and $\mathbf{B}_\omega(\mathbf{r},t) = \mathbf{B}_0(\omega)\mathrm{e}^{\mathrm{i}\frac{\omega}{c}[\mathbf{n}(\omega)\cdot\mathbf{r}-ct]}$ is the magnetic induction field. At finite frequencies, we can use μ_0 instead of the permeability tensor $\boldsymbol{\mu}$ [47–50].

The polar Kerr geometry, and a possible nonmagnetic optical anisotropy only in the xy plane, require that the dielectric tensor of the sample (magneto-optic medium), $\boldsymbol{\epsilon}(\omega)$, describing the relation between the electric and electric displacement fields, $\mathbf{D}^a_0(\omega) = \varepsilon_0\boldsymbol{\epsilon}(\omega)\cdot\mathbf{E}_0(\omega)$, has this generic form

$$\boldsymbol{\epsilon}(\omega) = \begin{pmatrix} \epsilon_{xx}(\omega) & \epsilon_{xy}(\omega) & 0 \\ \epsilon_{yx}(\omega) & \epsilon_{yy}(\omega) & 0 \\ 0 & 0 & \epsilon_{zz}(\omega) \end{pmatrix}. \tag{B7}$$

Then, Eq. (B4) implies that $E^{i'}_{0z}(\omega) = E^r_{0z}(\omega) = 0$.

Applying the curl ($\nabla\times$) to Eq. (B5) and using Eq. (B6), one can straightforwardly show that

$$(n^2(\omega)\mathbf{1} - \boldsymbol{\epsilon}(\omega))\cdot\mathbf{E}^r_0(\omega) = 0. \tag{B8}$$

Equation (B8) being valid for any $\mathbf{E}^i_0(\omega)$ and, consequently, for any $\mathbf{E}^r_0(\omega)$, it requires that

$$\det(n^2(\omega)\mathbf{1} - \boldsymbol{\epsilon}(\omega)) = 0, \tag{B9}$$

which gives the characteristics of the two principal propagation modes in the sample

$$n_\pm(\omega) = n_0(\omega)\sqrt{1 \pm \gamma(\omega)\sqrt{\alpha+\eta^2(\omega)+\gamma_{od}(\omega)}}, \tag{B10}$$

$$\underline{E}^r_{0y}(\omega) = \zeta_\pm(\omega)\underline{E}^r_{0x}(\omega), \tag{B11}$$

$$\zeta_\pm(\omega) = -\eta(\omega) \pm \sqrt{\alpha+\eta^2(\omega)+\gamma_{od}(\omega)}, \tag{B12}$$

where we have rewritten the components of the dielectric tensor in the following way:

$$\epsilon_{xx,yy}(\omega) = \epsilon_d(\omega) \pm \delta\epsilon_d(\omega), \tag{B13}$$

$$\epsilon_{xy}(\omega) = \epsilon_{od}(\omega), \tag{B14}$$

$$\epsilon_{yx}(\omega) = \alpha\epsilon_{od}(\omega) + \delta\epsilon_{od}(\omega), \quad \alpha = \pm 1, \tag{B15}$$

and used the following definitions:

$$n_0(\omega) = \sqrt{\epsilon_d(\omega)}, \tag{B16}$$

$$\gamma(\omega) = \frac{\epsilon_{od}(\omega)}{\epsilon_d(\omega)}, \tag{B17}$$

$$\gamma_{od}(\omega) = \frac{\delta\epsilon_{od}(\omega)}{\epsilon_{od}(\omega)}, \tag{B18}$$

$$\eta(\omega) = \frac{\delta\epsilon_d(\omega)}{\epsilon_{od}(\omega)}. \tag{B19}$$

These definitions allow to properly take into account (1) the two main conditions, linear birefringence ($\alpha = +1$, reciprocal anisotropy) and circular birefringence ($\alpha = -1$, gyrotropy), and (2) the actual relative relevance of the terms in the great majority of real experimental conditions where (for a given α) we have

$$|\delta\epsilon_d(\omega)| \ll |\epsilon_d(\omega)| \Rightarrow |\gamma_d(\omega)| \ll 1, \tag{B20}$$

$$\left.\begin{matrix} |\epsilon_{od}(\omega)| \ll |\epsilon_d(\omega)| \\ |\delta\epsilon_{od}(\omega)| \ll |\epsilon_{od}(\omega)| \end{matrix}\right\} \Rightarrow |\gamma_{od}(\omega)| \ll |\gamma_d(\omega)| \ll 1. \tag{B21}$$

Accordingly, we have

$$n_\pm(\omega) \cong n_0(\omega) \pm \frac{1}{2}\sqrt{\alpha}\gamma(\omega)n_0(\omega) \times \sqrt{1+\alpha\eta^2(\omega)}\left(1 + \frac{1}{2}\alpha\frac{\gamma_{od}(\omega)}{1+\alpha\eta^2(\omega)}\right) \tag{B22}$$

and

$$\zeta_\pm(\omega) \cong -\eta(\omega) \pm \sqrt{\alpha}\sqrt{1+\alpha\eta^2(\omega)}\left(1 + \frac{1}{2}\alpha\frac{\gamma_{od}(\omega)}{1+\alpha\eta^2(\omega)}\right). \tag{B23}$$

The approximate formulas take into account that by a proper rotation of the coordinate system around the z axis [of an angle $\theta = \frac{1}{2}\arctan(\frac{2\eta(\omega)}{1+\alpha+\gamma_{od}(\omega)})$ with respect to the x axis], we can reduce $\delta\epsilon_d(\omega)$, and, accordingly, also $\eta(\omega)$, to zero, moving the anisotropy of the diagonal elements to a symmetric component of the off-diagonal elements. The expressions of $\zeta_\pm(\omega)$ clarify why the sign of α determines the linearity [$\alpha = +1 \Rightarrow \zeta_\pm(\omega)$ predominatly real] or the circularity [$\alpha = -1 \Rightarrow \zeta_\pm(\omega)$ predominantly imaginary] of the birefringence.

Now, any incident wave can be formally decomposed in the two principal propagation modes in the sample

$$\mathbf{E}_0^i(\omega) = [1 - w(\omega)]\mathbf{E}_0^{i+}(\omega) + w(\omega)\mathbf{E}_0^{i-}(\omega), \tag{B24}$$

$$\mathbf{E}_0^{i+}(\omega) = [1, \zeta_+(\omega)]E_{0x}^i(\omega), \tag{B25}$$

$$\mathbf{E}_0^{i-}(\omega) = [1, \zeta_-(\omega)]E_{0x}^i(\omega), \tag{B26}$$

$$w(\omega) = \frac{\zeta(\omega) - \zeta_+(\omega)}{\zeta_-(\omega) - \zeta_+(\omega)}, \tag{B27}$$

$$\zeta(\omega) = \frac{E_{0y}^i(\omega)}{E_{0x}^i(\omega)}, \tag{B28}$$

that allows us to use the Fresnel relations for normal incidence [43–46] to easily compute the reflected wave, as the two principal propagation modes will be reflected with the following coefficients:

$$\mathbf{E}_0^{i'\pm}(\omega) = r_\pm(\omega)\mathbf{E}_0^{i\pm}(\omega), \tag{B29}$$

$$r_\pm(\omega) = \frac{1 - n_\pm(\omega)}{1 + n_\pm(\omega)}, \tag{B30}$$

that, to the first order in $\gamma(\omega)$ and $\gamma_{od}(\omega)$, assume the following expressions:

$$r_\pm(\omega) \cong r_0(\omega) \mp \sqrt{\alpha}\gamma(\omega)\frac{n_0(\omega)}{[1 + n_0(\omega)]^2} \times \sqrt{1 + \alpha\eta^2(\omega)}\left(1 + \frac{1}{2}\alpha\frac{\gamma_{od}(\omega)}{1 + \alpha\eta^2(\omega)}\right), \tag{B31}$$

where $r_0(\omega) = \frac{1-n_0(\omega)}{1+n_0(\omega)}$. Accordingly, the reflected wave reads as

$$E_{0x}^{i'}(\omega) = \{[1 - w(\omega)]r_+(\omega) + w(\omega)r_-(\omega)\}E_{0x}^i(\omega),$$

$$E_{0y}^{i'}(\omega) = [1 - w(\omega)]r_+(\omega)\zeta_+(\omega)E_{0x}^i(\omega) \tag{B32}$$

$$+ w(\omega)r_-(\omega)\zeta_-(\omega)E_{0x}^i(\omega), \tag{B33}$$

and we have, to the first order in $\gamma_{od}(\omega)$,

$$E_{0x}^{i'}(\omega) = r_0(\omega)E_{0x}^i(\omega) \tag{B34}$$

$$+ \gamma(\omega)\frac{n_0(\omega)}{[1 + n_0(\omega)]^2}[\zeta(\omega) - \eta(\omega)]E_{0x}^i(\omega), \tag{B35}$$

$$E_{0y}^{i'}(\omega) = \zeta(\omega)r_0(\omega)E_{0x}^i(\omega) \tag{B36}$$

$$+ \gamma(\omega)\eta(\omega)[\zeta(\omega) - \eta(\omega)]\frac{n_0(\omega)}{[1 + n_0(\omega)]^2}E_{0x}^i(\omega) \tag{B37}$$

$$+ \gamma(\omega)\frac{n_0(\omega)}{[1 + n_0(\omega)]^2}[\alpha + \eta^2(\omega) + \gamma_{od}(\omega)]E_{0x}^i(\omega), \tag{B38}$$

that defines the following Jones (reflection) matrix:

$$r_{xx}(\omega) = r_0(\omega)\left(1 - \eta(\omega)\gamma(\omega)\frac{n_0(\omega)}{1 - n_0^2(\omega)}\right), \tag{B39}$$

$$r_{xy}(\omega) = r_0(\omega)\gamma(\omega)\frac{n_0(\omega)}{1 - n_0^2(\omega)}, \tag{B40}$$

$$r_{yx}(\omega) = r_0(\omega)\gamma(\omega)[\alpha + \gamma_{od}(\omega)]\frac{n_0(\omega)}{1 - n_0^2(\omega)}, \tag{B41}$$

$$r_{yy}(\omega) = r_0(\omega)\left(1 + \eta(\omega)\gamma(\omega)\frac{n_0(\omega)}{1 - n_0^2(\omega)}\right). \tag{B42}$$

We can now compute the Kerr rotation angle [12,14,18,48,50–54] for a linear polarization along the x axis [$E_{0y}^i(\omega) = 0 \Rightarrow \zeta(\omega) = 0$],

$$\theta_{\mathrm{K}}^{\phi=0}(\omega) = \Re \arctan\frac{r_{yx}(\omega)}{r_{xx}(\omega)}, \tag{B43}$$

where ϕ is the angle formed by the polarization with the x axis. Up to the first order in $\gamma(\omega)$ and using that $\arctan(x) \simeq x$ for $|x| \ll 1$, $\theta_{\mathrm{K}}^{\phi=0}(\omega)$ read as

$$\theta_{\mathrm{K}}^{\phi=0}(\omega) = \Re\left(\gamma(\omega)[\alpha + \gamma_{od}(\omega)]\frac{n_0(\omega)}{1 - n_0^2(\omega)}\right) = \Re\left[\frac{\epsilon_{yx}(\omega)}{\sqrt{\epsilon_d(\omega)}[1 - \epsilon_d(\omega)]}\right]. \tag{B44}$$

For any other polarization angle ϕ, we can obtain the Kerr rotation angle by rotating the coordinate system in order to have the actual polarization to coincide with the new x axis and use the formulas just derived. This would require to rotate accordingly the dielectric tensor

$$\epsilon_{xx}^\phi = \epsilon_{xx}\cos^2\phi + (\epsilon_{xy} + \epsilon_{yx})\sin\phi\cos\phi + \epsilon_{yy}\sin^2\phi, \tag{B45}$$

$$\epsilon_{xy}^\phi = \epsilon_{xy}\cos^2\phi - \epsilon_{yx}\sin^2\phi + (\epsilon_{yy} - \epsilon_{xx})\sin\phi\cos\phi, \tag{B46}$$

$$\epsilon_{yx}^\phi = \epsilon_{yx}\cos^2\phi - \epsilon_{xy}\sin^2\phi + (\epsilon_{yy} - \epsilon_{xx})\sin\phi\cos\phi, \tag{B47}$$

$$\epsilon_{yy}^\phi = \epsilon_{xx}\sin^2\phi - (\epsilon_{xy} + \epsilon_{yx})\sin\phi\cos\phi + \epsilon_{yy}\cos^2\phi, \tag{B48}$$

that gives

$$\theta_{\mathrm{K}}^\phi(\omega) = \Re\left[\frac{\epsilon_{yx}^\phi(\omega)}{\sqrt{\epsilon_d(\omega)}[1 - \epsilon_d(\omega)]}\right], \tag{B49}$$

where $\epsilon_d(\omega)$, being half of the trace of the dielectric tensor, is an invariant under such a rotation.

According to this, the Kerr rotation angle is finite, with opposite signs, in both standard cases: for a mainly [$|\delta\epsilon_{od}(\omega)| \ll |\epsilon_{od}(\omega)|$] linear birefringent ($\alpha = +1$) sample and for a mainly circular birefringent ($\alpha = -1$) sample. On the other hand, in the case of pure linear birefringence [$\alpha = +1$, $|\delta\epsilon_{od}(\omega)| = 0$, reciprocal anisotropy: $\epsilon_{yx}(\omega) = \epsilon_{xy}(\omega)$], the Kerr rotation angle can be reduced to zero by choosing appropriately the impinging linear polarization, i.e., along the x axis of the coordinate system in which the dielectric tensor of the sample can be made diagonal, while in the case of mainly circular birefringence [$\alpha = -1$, $|\delta\epsilon_{od}(\omega)| \ll |\epsilon_{od}(\omega)|$, quasi gyrotropy: $\epsilon_{yx}(\omega) \cong -\epsilon_{xy}(\omega)$], the Kerr rotation angle cannot be reduced to zero by any choice of the linear polarization. This occurrence makes the latter case, quasi gyrotropy, much more relevant and interesting as, in this case, the Kerr rotation angle (1) becomes a fundamental measure of the gyrotropic magneto-optical response of the system, beyond standard linear birefringence, and (2) reveals to be an invariant for certain

magnetic semiconductors (usual ingredients are a finite spin-orbit coupling and broken time-reversal symmetry) in the same line as the Chern number is for topological insulators.

Now, while theoretically, to check the (magneto-optical) gyrotropy of a sample is enough to compute the degree of antisymmetric anisotropy through the definition of the polar (magneto-optical) Kerr rotation angle

$$\theta_{\mathrm{K}}(\omega) = \Re\left[\frac{\epsilon_{yx}(\omega) - \epsilon_{xy}(\omega)}{2\sqrt{\epsilon_d(\omega)}[1 - \epsilon_d(\omega)]}\right], \tag{B50}$$

experimentally, we need to average over all possible linear polarizations to integrate out the linear birefringence, i.e., the symmetric anisotropy component, and to single out the circular birefringence, i.e., the antisymmetric anisotropy component [55]. Such an averaging procedure results in

$$\bar{\theta}_{\mathrm{K}}(\omega) = \frac{1}{2\pi}\int_0^{2\pi} \theta_{\mathrm{K}}^{\phi}(\omega) d\phi = \theta_{\mathrm{K}}(\omega), \tag{B51}$$

which in turn justifies the definition of the polar Kerr rotation angle given in Eq. (B50).

[1] T. Brabec and F. Krausz, Rev. Mod. Phys. **72**, 545 (2000).
[2] F. Krausz and M. Ivanov, Rev. Mod. Phys. **81**, 163 (2009).
[3] F. Krausz and M. I. Stockman, Nat. Photonics **8**, 205 (2014).
[4] F. Calegari, G. Sansone, S. Stagira, C. Vozzi, and M. Nisoli, J. Phys. B: At. Mol. Opt. Phys. **49**, 062001 (2016).
[5] M. Gandolfi, G. L. Celardo, F. Borgonovi, G. Ferrini, A. Avella, F. Banfi, and C. Giannetti, Phys. Scr. **92**, 034004 (2017).
[6] R. Borrego-Varillas, M. Lucchini, and M. Nisoli, Rep. Prog. Phys. **85**, 066401 (2022).
[7] G. Inzani, L. Adamska, A. Eskandari-asl, N. Di Palo, G. L. Dolso, B. Moio, L. J. D'Onofrio, A. Lamperti, A. Molle, R. Borrego-Varillas, *et al.*, Nat. Photonics **17**, 1059 (2023).
[8] G. Inzani, A. Eskandari-asl, L. Adamska, B. Moio, G. L. Dolso, N. D. Palo, L. J. D'Onofrio, A. Lamperti, A. Molle, C. A. Rozzi, R. Borrego-Varillas, M. Nisoli, S. Pittalis, A. Avella, and M. Lucchini, Il Nuovo Cimento C **46**, 110 (2023).
[9] M. Zürch, H.-T. Chang, L. J. Borja, P. M. Kraus, S. K. Cushing, A. Gandman, C. J. Kaplan, M. H. Oh, J. S. Prell, D. Prendergast, C. D. Pemmaraju, D. M. Neumark, and S. R. Leone, Nat. Commun. **8**, 15734 (2017).
[10] C. J. Kaplan, P. M. Kraus, A. D. Ross, M. Zürch, S. K. Cushing, M. F. Jager, H.-T. Chang, E. M. Gullikson, D. M. Neumark, and S. R. Leone, Phys. Rev. B **97**, 205202 (2018).
[11] L. Perfetti, P. A. Loukakos, M. Lisowski, U. Bovensiepen, M. Wolf, H. Berger, S. Biermann, and A. Georges, New J. Phys. **10**, 053019 (2008).
[12] G. P. Zhang, W. Hübner, G. Lefkidis, Y. Bai, and T. F. George, Nat. Phys. **5**, 499 (2009).
[13] K. Sato and T. Ishibashi, Front. Phys. **10**, 946515 (2022).
[14] E. Beaurepaire, J.-C. Merle, A. Daunois, and J.-Y. Bigot, Phys. Rev. Lett. **76**, 4250 (1996).
[15] A. V. Kimel, A. Kirilyuk, P. A. Usachev, R. V. Pisarev, A. M. Balbashov, and T. Rasing, Nature (London) **435**, 655 (2005).
[16] J. Wang, C. Sun, Y. Hashimoto, J. Kono, G. A. Khodaparast, Ł. Cywiński, L. Sham, G. D. Sanders, C. J. Stanton, and H. Munekata, J. Phys.: Condens. Matter **18**, R501 (2006).
[17] A. Kirilyuk, A. V. Kimel, and T. Rasing, Rev. Mod. Phys. **82**, 2731 (2010).
[18] M. W. Wu, J. H. Jiang, and M. Q. Weng, Phys. Rep. **493**, 61 (2010).
[19] M. Hennecke, D. Schick, T. Sidiropoulos, F. Willems, A. Heilmann, M. Bock, L. Ehrentraut, D. Engel, P. Hessing, B. Pfau, *et al.*, Phys. Rev. Res. **4**, L022062 (2022).
[20] P. Němec, M. Fiebig, T. Kampfrath, and A. V. Kimel, Nat. Phys. **14**, 229 (2018).
[21] I. Gray, Q. Deng, Q. Tian, M. Chilcote, J. S. Dodge, M. Brahlek, and L. Wu, Appl. Phys. Lett. **125**, 212404 (2024).
[22] A. Eskandari-asl, J. I. Facio, O. Janson, A. Avella, and J. van den Brink, Phys. Rev. B **112**, 024401 (2025).
[23] T. Kampfrath, M. Battiato, P. Maldonado, G. Eilers, J. Nötzold, S. Mährlein, V. Zbarsky, F. Freimuth, Y. Mokrousov, S. Blügel, *et al.*, Nat. Nanotechnol. **8**, 256 (2013).
[24] T.-S. Zeng, D. N. Sheng, and W. Zhu, Phys. Rev. B **101**, 035138 (2020).
[25] U. De Giovannini, G. Brunetto, A. Castro, J. Walkenhorst, and A. Rubio, ChemPhysChem **14**, 1298 (2013).
[26] U. De Giovannini, H. Hubener, and A. Rubio, Nano Lett. **16**, 7993 (2016).
[27] U. De Giovannini and A. Castro, Attosecond Mol. Dyn. **13**, 424 (2018).
[28] F. Schlaepfer, M. Lucchini, S. A. Sato, M. Volkov, L. Kasmi, N. Hartmann, A. Rubio, L. Gallmann, and U. Keller, Nat. Phys. **14**, 560 (2018).
[29] S. A. Sato, M. Lucchini, M. Volkov, F. Schlaepfer, L. Gallmann, U. Keller, and A. Rubio, Phys. Rev. B **98**, 035202 (2018).
[30] L. Broers and L. Mathey, Phys. Rev. Res. **4**, 013057 (2022).
[31] A. Eskandari-asl and A. Avella, Phys. Rev. B **110**, 094309 (2024).
[32] A. Eskandari-asl and A. Avella, Phys. Rev. A **110**, 043520 (2024).
[33] A. Eskandari-Asl and A. Avella, Materials **18**, 1310 (2025).
[34] A. Eskandari-asl and A. Avella, in *Advances in Ultrafast Condensed Phase Physics IV* (SPIE, Bellingham, 2024), Vol. 12992, pp. 65–68
[35] M. Schüler, J. A. Marks, Y. Murakami, C. Jia, and T. P. Devereaux, Phys. Rev. B **103**, 155409 (2021).
[36] B. Koopmans, M. van Kampen, J. T. Kohlhepp, and W. J. M. de Jonge, Phys. Rev. Lett. **85**, 844 (2000).
[37] P. M. Oppeneer and A. Liebsch, J. Phys.: Condens. Matter **16**, 5519 (2004).
[38] S. Mukamel, *Principles of Nonlinear Optical Spectroscopy*, Oxford Series in Optical and Imaging Sciences (Oxford University, New York, 1995).
[39] J. W. Freeland, R. H. Kodama, M. Vedpathak, S. C. Erwin, D. J. Keavney, R. Winarski, P. Ryan, and R. A. Rosenberg, Phys. Rev. B **70**, 033201 (2004).
[40] ELK Developers, The Elk code, http://elk.sourceforge.net/ (2000).
[41] G. Pizzi, V. Vitale, R. Arita, S. Blügel, F. Freimuth, G. Géranton, M. Gibertini, D. Gresch, C. Johnson, T. Koretsune, *et al.*, J. Phys.: Condens. Matter **32**, 165902 (2020).
[42] A. Eskandari-asl and A. Avella, Magneto-optical Kerr effect in pump-probe setups [Data set], In Physical Review A, American Physical Society, Zenodo (2026), https://doi.org/10.5281/zenodo.18241512.

[43] J. D. Jackson, *Classical Electrodynamics*, 3rd ed. (Wiley, New York, 1998).
[44] M. Born and E. Wolf, *Principles of Optics*, 7th ed. (Cambridge University, Cambridge, 1999).
[45] A. Zangwill, *Modern Electrodynamics* (Cambridge University, Cambridge, 2012).
[46] E. Hecht, *Optics*, 5th ed. (Pearson, London, 2017).
[47] L. Landau and E. M. Lifshitz, *Electrodynamics of Continuous Media*, Course of Theoretical Physics (Pergamon, New York, 1960).
[48] P. S. Pershan, J. Appl. Phys. **38**, 1482 (1967).
[49] O. Dolgov and E. Maksimov, in *The Dielectric Function of Condensed Systems*, Modern Problems in Condensed Matter Sciences, Vol. 24, edited by L. Keldysh, D. Kirzhnitz, and A. Maradudin (Elsevier, New York, 1989), pp. 221–298.
[50] P. Oppeneer, in *Handbook of Magnetic Materials* (Elsevier, New York, 2001), Vol. 13, pp. 229–422.
[51] P. N. Argyres, Phys. Rev. **97**, 334 (1955).
[52] J. L. Erskine and E. A. Stern, Phys. Rev. B **8**, 1239 (1973).
[53] A. K. Zvezdin and V. A. Kotov, *Modern Magnetooptics and Magnetooptical Materials* (CRC Press, Boca Raton, 1997).
[54] Z. Q. Qiu and S. D. Bader, Rev. Sci. Instrum. **71**, 1243 (2000).
[55] M. Weber, S. Wust, L. Haag, A. Akashdeep, K. Leckron, C. Schmitt, R. Ramos, T. Kikkawa, E. Saitoh, M. Kläui, *et al.*, arXiv:2408.05187.